RSC Advances

PAPER

View Article Online
View Journal | View Issue

Cite this: *RSC Adv.*, 2017, **7**, 53145

Preparation and enhanced photocatalytic hydrogen-evolution activity of $ZnGa_2O_4$/N-rGO heterostructures†

X. P. Bai,[a] X. Zhao[b] and W. L. Fan *[a]

Semiconductor–graphene composites have been widely reported as photocatalysts for hydrogen generation. The structure of the semiconductor, intimate interfacial contact between the components, and high electrical conductivity of the catalyst support can affect the performance of semiconductor–graphene composite photocatalysts. We successfully synthesized size-controlled $ZnGa_2O_4$ nanospheres by adjusting the amount of surfactant trisodium citrate, and assembled size-controlled $ZnGa_2O_4$ nanospheres on the two-dimensional platform of an N-doped reduced graphene oxide (N-rGO) sheet through the conventional and efficient hydrothermal method, during which the intimate interfacial contact between $ZnGa_2O_4$ nanospheres and the N-rGO sheet are achieved. The obtained photocatalysts were characterized by X-ray powder diffraction, Raman spectroscopy, transmission electron microscopy, X-ray photoelectron spectroscopy, and ultraviolet visible diffuse reflectance spectroscopy. The photocatalytic activity of the prepared samples for H_2 evolution was tested using sodium sulfite as the sacrificial agent. The effects of the crystallinity, morphology, and specific surface area of the $ZnGa_2O_4$ samples on the rate of photocatalytic hydrogen production were studied. Considering the above three factors, the rate of H_2 production was highest when the diameter of the $ZnGa_2O_4$ spheres reached 230 nm. The rate of H_2 evolution of the $ZnGa_2O_4$/rGO and $ZnGa_2O_4$/N-rGO composites dramatically improved when compared with that of pure $ZnGa_2O_4$. $ZnGa_2O_4$/N-rGO had higher photocatalytic activity than $ZnGa_2O_4$/rGO because the nitrogen atoms in N-rGO could anchor the metal nanoparticles to form an intimate interfacial contact between N-rGO and $ZnGa_2O_4$, and N-rGO had higher electrical conductivity than rGO, resulting in more effective charge separation and transfer in the $ZnGa_2O_4$/N-rGO composites. This study offers a promising method to design more efficient graphene-based nanocomposite photocatalysts for enhancing photocatalytic activity.

Received 7th September 2017
Accepted 13th November 2017

DOI: 10.1039/c7ra09981a

rsc.li/rsc-advances

Introduction

Hydrogen has attracted increased attention in recent years as a renewable and clean energy carrier.[1–10] One of the best ways to produce hydrogen is photocatalytic water splitting under light irradiation, which offers a viable strategy to solve the energy crisis and environmental problems resulting from the burning of fossil fuels.[11] So far, much effort has been dedicated to the development of photocatalysts, and numerous active photocatalysts such as various oxide, sulfide, and oxynitride semiconductors have been reported.[12–17] Among them, metal oxides and their composites that contain metal cations with d^0 and d^{10} electronic configurations at the highest oxidation states are regarded as good photocatalysts for water splitting.[18,19] Zinc gallate ($ZnGa_2O_4$), a ternary metal-oxide-based spinel, has been widely used as a catalyst in air-pollution control,[20] wastewater treatment,[21] and water splitting.[22–24] However, the fast recombination of photogenerated charge carriers remains a major problem. Modulating the structure of the semiconductor, such as its crystallinity and morphology, and constructing semiconductor-matrix systems have proved to be efficient ways to retard the recombination of photogenerated electron–hole pairs.[25–33]

Graphene, a two-dimensional (2D) sheet of sp^2-hybridized carbon atoms, has been considered as an excellent catalyst support and electron-transport matrix because of its high surface area, electrical conductivity, and mobility of charge carriers.[34–40] So far, various semiconductor–graphene composite photocatalysts for hydrogen generation have been reported.[41–44] The hydrophilicity of GO can be used as a binder, which is

[a]*Key Laboratory for Colloid and Interface Chemistry of State Educating Ministry, School of Chemistry and Chemical Engineering, Shandong University, Jinan 250100, China. E-mail: fwl@sdu.edu.cn; Fax: +86-531-88364864; Tel: +86-531-88366330*

[b]*State Key Laboratory of Crystal Materials, Shandong University, Jinan 250100, China*

† Electronic supplementary information (ESI) available: The SEM images, FT-IR spectra and UV-vis spectra of the $ZnGa_2O_4$ with different size, the TEM and HRTEM images of the $ZnGa_2O_4$/rGO samples, the BET surface area of all samples, photocatalytic water splitting activity normalized by the BET surface areas of $ZnGa_2O_4$/rGO and $ZnGa_2O_4$/N-rGO composites. See DOI: 10.1039/c7ra09981a

necessary for the development of graphene-based composites for various applications.[45] However, reduced graphene oxide (rGO) does not exhibit high electronic conductivity because of damages to the sp^2-hybridized network. Generally speaking, heteroatom doping can dramatically alter the electrical properties of graphene,[46,47] and both theoretical and experiment studies have revealed that N doping can effectively modulate the chemical reactivity and electronic properties of graphene.[48,49] Since N doping can increase the electronic conductivity because nitrogen has stronger electronegativity than carbon and because of the conjugation between the graphene π-system and the nitrogen lone-pair electrons,[50] N-doped graphene has been used in lithium–ion batteries,[51] biosensors or chemical sensors,[52] and catalytic reactions including oxygen reduction[53] and degradation of organic contaminants.[54]

In this study, we successfully synthesized size-controlled $ZnGa_2O_4$ nanospheres composed of $ZnGa_2O_4$ particles by adjusting the amount of surfactant trisodium citrate. We assembled the size-controlled $ZnGa_2O_4$ nanospheres on the 2D platforms of N-doped reduced graphene oxide (N-rGO) sheets and rGO sheets through the conventional and efficient hydrothermal method. We then investigated the effects of the crystallinity and morphology of the semiconductor and the electrical conductivity of the catalyst support on the photocatalytic activity for hydrogen evolution. In addition, a possible photocatalytic mechanism of $ZnGa_2O_4$/N-rGO was explored.

Experimental

Preparation

The starting materials were $Ga(NO_3)_3 \cdot xH_2O$ (99.9%, Alfa Aesar Chemical Reagent Co., Ltd., China), graphene oxide powder (XFNANO Materials Tech. Co., China), and other reagents (Shanghai Sinopharm Chemical Reagent Co., Ltd., China). All chemicals were analytical grade and used without further purification.

Synthesis of $ZnGa_2O_4$ nanospheres

$ZnGa_2O_4$ nanospheres were synthesized by the conventional hydrothermal method. First, 0.298 g $Zn(NO_3)_2 \cdot 6H_2O$ was added 40 mL deionized water and 0.512 g $Ga(NO_3)_3 \cdot xH_2O$ was added 40 mL deionized water to obtained Zn^{2+} and Ga^{3+} solutions by stirring. The Ga^{3+} and Zn^{2+} solutions were mixed and stirred for 15 min, and then a certain amount of trisodium citrate ($C_6H_5Na_3O_7 \cdot 2H_2O$) was added, together with an ammonia solution (25.0 wt% NH_3) used to control the pH was 8.5. After stirring for an additional 20 min, the solution was transferred to a 100 mL Teflon autoclave, sealed, and heated at 200 °C for 24 h. The precipitated solid product was collected by centrifuging, washed, dried at 60 °C in air, and then calcined at 400 °C in air. Hereafter, the obtained samples are denoted as $ZnGa_2O_4$-*x*, where *x* represents the amount of trisodium citrate in grams.

Synthesis of N doped graphene oxide

Nitrogen-doped graphene oxide (NGO) was synthesized by a moderate refluxing process in an ammonia solution.[55] The ammonia solution (25.0 wt%, 0.3 mL) was mixed with an aqueous GO solution (0.2 wt%, 20.0 mL) by magnetic stirring at 80 °C for 8 h to obtain partly reduced NGO.

Synthesis of $ZnGa_2O_4$/rGO and $ZnGa_2O_4$/N-rGO composites

First, $ZnGa_2O_4$ nanospheres (0.120 g) were added to deionized water (30 mL) and sonicated for 30 min to obtain a homogeneous suspension. Next, 3 mL GO solution (1 mg mL^{-1}) or the NGO suspension (1 mg mL^{-1}) was added under magnetic stirring for 30 min. The suspension was then transferred to a 50 mL Teflon autoclave, sealed, and heated at 200 °C for 6 h. The precipitated solid product was collected by centrifuging, washed, and then dried at 60 °C in air. Hereafter, the obtained sample is denoted as $ZnGa_2O_4$/rGO (if prepared with the aqueous GO solution) or $ZnGa_2O_4$/N-rGO (if prepared with the NGO suspension). The synthesis parameters of the samples are listed in the Table S1.†

For comparison, the $ZnGa_2O_4$ nanospheres in deionized water and the $ZnGa_2O_4$ nanospheres in an ammonia solution (without the aqueous GO solution or the NGO suspension) were also transferred to a 50 mL Teflon-autoclave, sealed, and heated at 200 °C for 6 h. And the sample of $ZnGa_2O_4$ and N-rGO composites by stirred mixing 6 h was prepared, which based on the same weight ratio with the above $ZnGa_2O_4$/N-rGO.

Characterization

X-ray powder diffraction (XRD) measurements were performed on an X-ray diffractometer (D8 Advance, Bruker, Germany) with Cu K_α radiation ($\lambda = 1.54178$ Å). Scanning electron microscopy (SEM) was carried out with a field-emission scanning electron microscopy (FESEM; S-4800, Hitachi, Japan) at an accelerating voltage of 5 kV. The transmission electron microscope (TEM) images and high-resolution transmission electron microscope (HRTEM) images were obtained with an electron microscope (JEM 2100. JEOL, Japan) operating at an accelerating voltage of 200 kV. Raman spectroscopy was performed at room temperature by a Raman spectrometer (Nicolet 67000/NXR, ThermoFisher, USA) with a 532 nm Nd:YAG excitation source. X-ray photoelectron spectroscopy (XPS) measurements and valence-band X-ray photoelectron spectroscopy (VB XPS) measurements were performed on an X-ray photoelectron spectrometer (ESCALAB 250, ThermoFisher, USA) equipped with an Al K_α source. Photoluminescence (PL) spectra were obtained with a fluorescence spectrophotometer (F-4500, Hitachi High-Technologies, Japan) at the emission wavelength of 310 nm. Ultraviolet-visible (UV-vis) diffuse-reflectance spectra (DRS) were recorded on a UV-vis spectrophotometer (UV-2550, Shimadzu, Japan), with $BaSO_4$ used as the reference sample. The Brunauer–Emmett–Teller (BET) surface area of each sample was obtained on a surface area analyzer (ASAP 2020, Micromeritics, USA) at the liquid-nitrogen temperature. Fourier transform infrared (FT-IR) spectra were obtained with an infrared spectrometer (NEXUS 670, Thermo Nicolet, USA).

Photoelectrochemical characteristics

The photoelectrochemical characteristics of the samples were measured with an electrochemistry potentiostat (CHI 660D,

Shanghai Chenhua Limited, China) using a homemade three-electrode cell with Ag/AgCl as the reference electrode and a Pt wire as the counter electrode. An aqueous Na_2SO_4 (0.5 M) solution was used as the electrolyte under UV light irradiation from a 300 W xenon lamp (PLS-SXE300CUV, Beijing Perfect Light Co., Ltd., China). For the fabrication of the photoanode, 10 mg of each sample was added to a certain amount of dimethyl formamide (DMF) and ground for 15 min to obtain slurry. The slurry was then spread on a 15 mm × 20 mm indium–tin oxide (ITO) conducting glass and then dried under ambient conditions.

Photocatalytic activity evaluation

Hydrogen production reactions were carried out at 5 °C in a closed-circulation gas system. First, 0.05 g of sample was dispersed in 100 mL of an aqueous 0.05 M Na_2SO_3 solution as the sacrificial reagent in a borosilicate glass reactor equipped with a quartz lid for light penetration. A suitable amount of H_2PtCl_6 (Pt content: 1 wt%) was then added to the solution as the co-catalyst. The photoreactor containing the cocatalyst, sacrificial reagent, and photocatalyst was then sonicated for several minutes to allow the suspension to mix uniformly. Before illumination, nitrogen gas was purged through the suspension for 0.5 h. A 300 W xenon lamp ($\lambda \geq 250$ nm, PLS-SXE300CUV, Beijing Perfect Light Co., Ltd., China) was used as UV light source (15 cm far away from the photocatalytic reactor). The focused intensity on the flask was detected to be 89.68 mW cm^{-2} by UV radiometer (UV-A 141108). The amount of hydrogen produced was analyzed by a gas chromatograph (GC-7806 TCD) using 5 Å molecular sieve columns and N_2 as the carrier gas. The apparent quantum efficiency (QE) was measured under the similar photocatalytic reaction conditions using four low power UV-LEDs (3 W, 365 nm, Shenzhen LAMPLIC Science Co. Ltd. China) and an UV radiometer (UV-A 141108). The four low power UV-LEDs were used as light sources (1 cm away from the reactor in four different directions). The focused intensity and areas on the flask for each UV-LED was detected to be 75.61 mW cm^{-2} and 1 cm^2, respectively. According to eqn (1),[43] the QE was measured and calculated:

$$\mathrm{QE}\ [\%] = \frac{2 \times \text{number of evolved } H_2 \text{ molecules}}{\text{number of incident photons}} \times 100\% \quad (1)$$

Results and discussion

Structure and morphology of the $ZnGa_2O_4$, $ZnGa_2O_4$/rGO and $ZnGa_2O_4$/N-rGO composites

The phase crystallinity and purity of the precursor and as-prepared samples were determined by analyzing the XRD measurements. Fig. 1a shows the XRD patterns of the as-prepared $ZnGa_2O_4$ samples with different amounts of the surfactant trisodium citrate, which match the powder diffraction pattern of cubic $ZnGa_2O_4$ (JCPDS card no. 38-1240). The absence of other XRD features indicates the high purity of the as-prepared $ZnGa_2O_4$ samples. The diffraction patterns are weak for the sample prepared without added surfactant, indicating that the crystallinity of $ZnGa_2O_4$-0 was low. Furthermore, the diffraction patterns of the samples with increasing amount of surfactant are stronger, indicating that the crystallinity of $ZnGa_2O_4$-x increases with increasing surfactant content.[56] This phenomenon may be ascribed to the structure-directing reagent trisodium citrate, that could form Zn^{2+}–Cit^{3-}–Ga^{3+} complexes to control the nucleation and growth of the crystals, resulting in the $ZnGa_2O_4$ particles assembling into nanospheres[57] and increased crystallinity. The formation of $ZnGa_2O_4$ nanospheres was confirmed by SEM and TEM observations. The crystallinity of the $ZnGa_2O_4$ nanospheres did not exhibit obvious changes when the amount of trisodium citrate was above 0.35 g. Fig. 1b shows the XRD patterns of GO, NGO, $ZnGa_2O_4$-0.30 (ZGO), $ZnGa_2O_4$-0.30/rGO (ZGO/rGO), and $ZnGa_2O_4$-0.30/N-rGO (ZGO/N-rGO). The GO plates showed a sharp diffraction peak at $2\theta = 10.8°$, which is indexed to the (001) crystal plane. However, NGO exhibited an XRD peak corresponding to the (002) plane at 26.3°, indicating that part of GO was mildly reduced during the moderate refluxing process in the ammonia solution.[55] Obviously, the diffraction peaks of the ZGO/rGO and ZGO/N-rGO composites are in good agreement with those of cubic $ZnGa_2O_4$ (JCPDS card no. 38-1240), which has the same composition as pure $ZnGa_2O_4$. No shift in the diffraction peaks of the ZGO/rGO and ZGO/N-rGO composites were observed

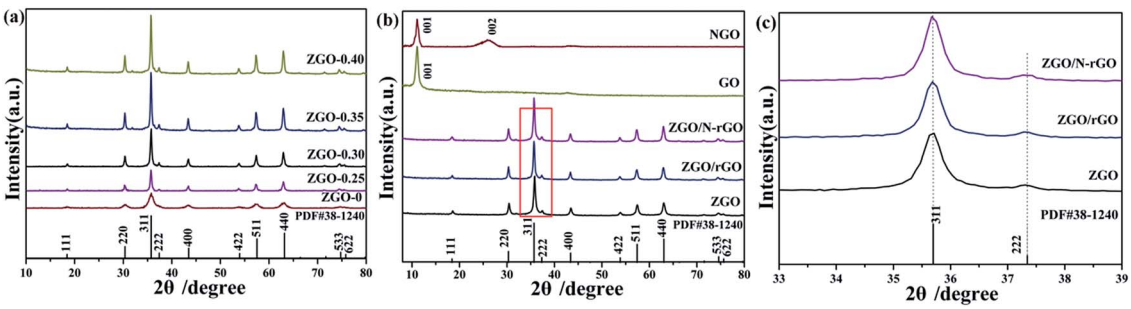

Fig. 1 XRD patterns of the precursor and as-prepared samples of $ZnGa_2O_4$ with different amounts of the surfactant trisodium citrate: (a) $ZnGa_2O_4$-0, $ZnGa_2O_4$-0.25, $ZnGa_2O_4$-0.30, $ZnGa_2O_4$-0.35, and $ZnGa_2O_4$-0.40 (the powder diffraction pattern of cubic $ZnGa_2O_4$ (JCPDS card no. 38-1240) is included for comparison); (b) GO, NGO, $ZnGa_2O_4$-0.30 (ZGO), $ZnGa_2O_4$-0.30/rGO (ZGO/rGO), and $ZnGa_2O_4$-0.30/N-rGO (ZGO/N-rGO); (c) $ZnGa_2O_4$-0.30 (ZGO), $ZnGa_2O_4$-0.30/rGO (ZGO/rGO) and $ZnGa_2O_4$-0.30/N-rGO (ZGO/N-rGO).

when compared with of the peaks of pure $ZnGa_2O_4$ (Fig. 1c), indicating that there were no changes in the lattice structure of $ZnGa_2O_4$ in the ZGO/rGO and ZGO/N-rGO composites.[58] This result suggests that rGO and N-rGO were not inserted in the lattice of $ZnGa_2O_4$, which means that $ZnGa_2O_4$ was deposited on the surface of rGO and N-rGO. The absence of the rGO and N-rGO diffraction peaks in the patterns of the ZGO/rGO and ZGO/N-rGO composites can be ascribed to the low content (2%) of rGO and N-rGO.[59]

The morphology of the as-prepared $ZnGa_2O_4$ samples ($ZnGa_2O_4$-x) prepared with different amounts of trisodium citrate (x in grams) was investigated with TEM and SEM, and the results are shown in Fig. 2 and S1,† respectively. It can be seen that with the increase in the amount of trisodium citrate amount, the diameter of $ZnGa_2O_4$ spheres increased. The morphology of the $ZnGa_2O_4$ samples was characterized by irregular particles when the amount of trisodium citrate used was below 0.25 g (Fig. 2a–d). Further increase in the amount of trisodium citrate used (0.30 g) led to the assembling of $ZnGa_2O_4$ particles into nanospheres with diameters of about 80 nm (Fig. 2e and f). The diameter of the $ZnGa_2O_4$ nanospheres was about 230 and 260 nm when the amount of trisodium citrate used was 0.35 g (Fig. 2g and h) and 0.40 g (Fig. 2i and j), respectively. These results indicate that we successfully synthesized size-controlled $ZnGa_2O_4$ nanospheres by adjusting the amount of trisodium citrate.

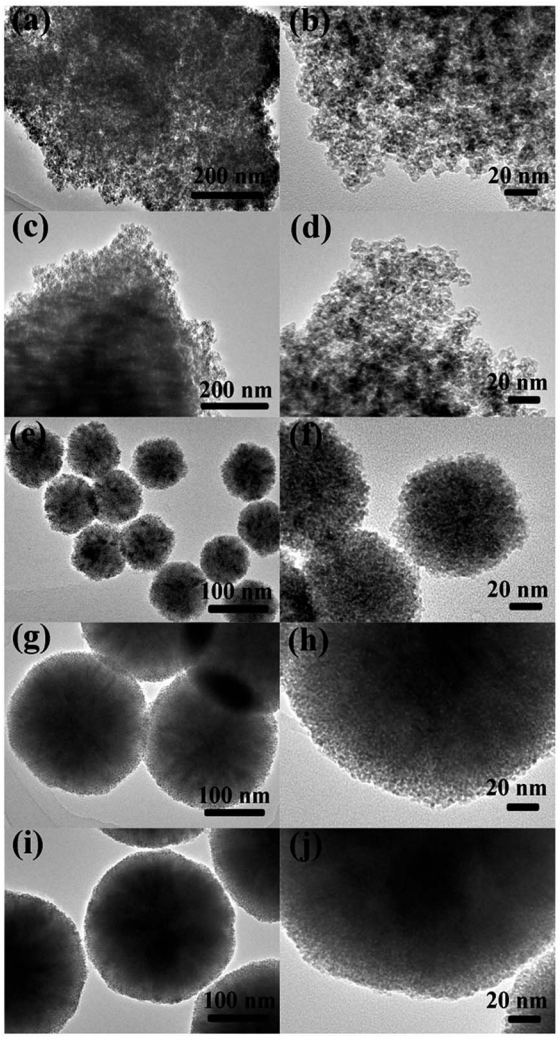

Fig. 2 TEM images of $ZnGa_2O_4$ samples with different amount of surfactant trisodium citrate: (a, b) $ZnGa_2O_4$-0; (c, d) $ZnGa_2O_4$-0.25; (e, f) $ZnGa_2O_4$-0.30; (g, h) $ZnGa_2O_4$-0.35 and (i, j) $ZnGa_2O_4$-0.40.

The morphology of the $ZnGa_2O_4$/N-rGO and $ZnGa_2O_4$/rGO composites are shown in Fig. 3 and S2.† Fig. 3 shows typical TEM and HRTEM images of the $ZnGa_2O_4$-0.25/N-rGO, $ZnGa_2O_4$-0.30/N-rGO, and $ZnGa_2O_4$-0.35/N-rGO samples, in which we can clearly see that $ZnGa_2O_4$ was deposited on the surface of the N-rGO sheet. The lattice fringe of $d = 0.34$ nm corresponds to the (002) plane of N-rGO,[59] and the lattice spacing of $d = 0.25$ nm matches well with the (311) plane of $ZnGa_2O_4$.[57] The $ZnGa_2O_4$ aggregated on the surface of the N-rGO sheet when $ZnGa_2O_4$ consisted of irregular particles (Fig. 3a), which was an adverse effect on charge separation and charge transfer. Fig. 3c and e show $ZnGa_2O_4$ uniformly dispersed on the N-rGO sheet when the $ZnGa_2O_4$ particles assembled to form nanospheres, which could promote charge separation and thus enhance the catalytic activity. These results indicate that we successfully assembled $ZnGa_2O_4$ on the 2D platform of the N-rGO sheet.

Fig. 4 shows the FT-IR spectra of GO, NGO, ZGO, ZGO/rGO, and ZGO/N-rGO. In the FT-IR spectra of the GO and NGO, the bands at 1726, 1623, 1560 and 1052 cm^{-1} are ascribed to C=O in COOH stretching, aromatic C=C skeletal vibration, and alkoxy C–O stretching, respectively.[54] In the FT-IR spectrum of NGO, the broad band centered at 1000–1240 cm^{-1} includes alkoxy C–O (1052 cm^{-1}) and epoxy C–O (1226 cm^{-1}) stretching vibrations, and the peak of C=O at 1726 cm^{-1} stretching is

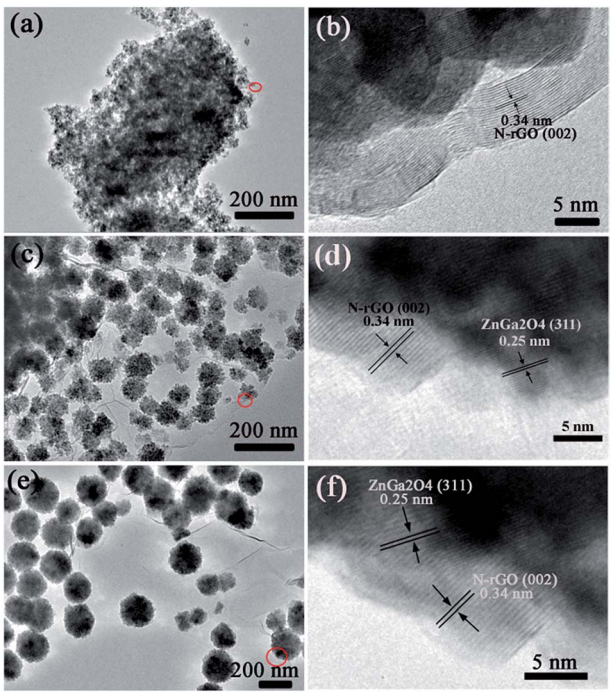

Fig. 3 TEM and HRTEM images of the samples: (a, b) $ZnGa_2O_4$-0.25/N-rGO; (c, d) $ZnGa_2O_4$-0.30/N-rGO; (e, f) $ZnGa_2O_4$-0.35/N-rGO.

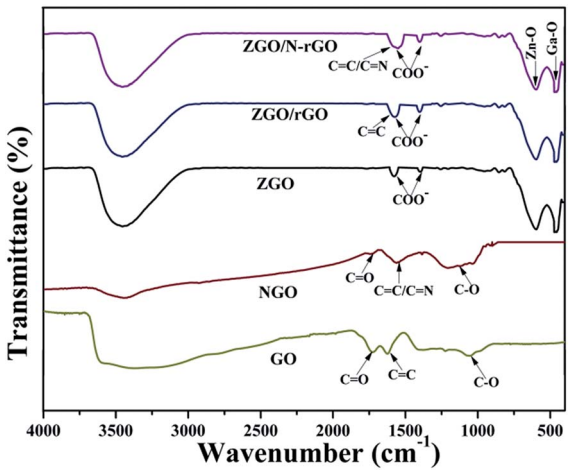

Fig. 4 FT-IR spectra of the precursor and as-prepared samples: GO, NGO, ZGO, ZGO/rGO and ZGO/N-rGO.

significantly diminished, implying that GO was mildly reduced. Owing to the overlapping C=N (1572 cm^{-1}) and C=C peaks and the relatively low ratio of N to C atoms, it was difficult to identify the C=N signal by FT-IR.[60] In the FT-IR spectra of ZGO/rGO and ZGO/N-rGO composites, the peaks of C=O stretching at 1726 cm^{-1} and alkoxy C–O stretching at 1052 cm^{-1} are absent, indicating that there was reduced graphene oxide (rGO) in the ZGO/rGO and ZGO/N-rGO composites. These results were further confirmed by Raman and XPS observations.

In order to confirm that there was reduced graphene oxide in the ZGO/rGO and ZGO/N-rGO composites, Raman spectra of GO, ZGO/rGO, ZGO/N-rGO, and NGO were obtained. It can be seen in Fig. 5 that all samples exhibited two typical peaks (D band and G band). In Raman spectroscopy, the D band is related to structural disorder and defects in graphene, and the G band is due to stretching of sp^2-hybridized C=C.[61–63] Both bands can be modified by doping, with the D and G bands shifting toward lower frequencies upon N-doping,[50] which has also been observed in N-doped graphene oxide derived from a moderate refluxing treatment in an ammonia solution of

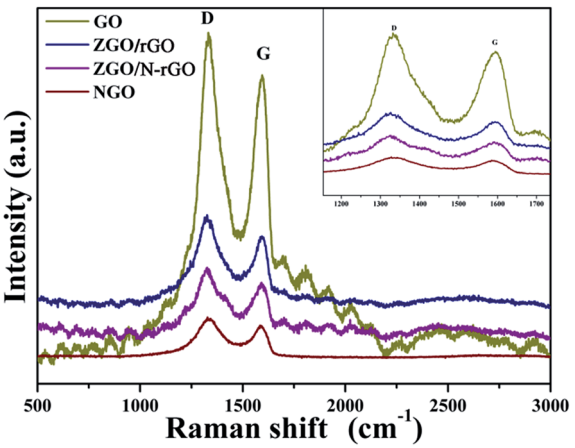

Fig. 5 Raman spectra of GO, ZGO/rGO, ZGO/N-rGO and NGO.

graphene oxide. It has been reported that the Raman shifts of the D and G bands are slightly blue-shifted when GO is reduced to rGO.[64,65] Similar trends were observed in this study: as GO transformed to ZGO/rGO, the D band shifted from 1332 to 1325 cm^{-1}, whereas the G band shifted from 1595 to 1593 cm^{-1}; for the transformation from NGO to ZGO/N-rGO, the D band shifted from 1330 to 1326 cm^{-1}, whereas the G band shifted from 1588 to 1584 cm^{-1}. Compared with the Raman spectra of GO and NGO, an increase in the ratio between the intensities of D and G bands (I_D/I_G) was observed in the spectra of the composites. The values of I_D/I_G for GO and NGO was 1.15 and 1.19, respectively, while it increased to 1.28 and 1.29 for ZGO/rGO and ZGO/N-rGO, thus confirming the existence of reduced graphene oxide sheets in the ZGO/rGO and ZGO/N-rGO composites[43,66] and indicating the reduction of the exfoliated GO.[67] In addition, the values of I_D/I_G of NGO and ZGO/N-rGO were higher than those of GO and ZGO/rGO, thereby implying that nitrogen was successfully introduced into GO.[68] This result was further confirmed by XPS analysis.

XPS was conducted to characterize the chemical composition and surface chemical states of the as-prepared samples. As shown in Fig. 6, the C 1s XPS peaks of GO centered at 284.5, 286.7 and 288.5 eV are assigned to the C–C bond, C–O/C=O bond (epoxy, hydroxyl, and carbonyl) and O–C=O bond (carboxyl), respectively,[69,70] which clearly indicate a high degree of oxidation. In the C 1s XPS spectrum of ZGO/rGO, the intensity of the peak for the O–C=O bond is much lower than that in the spectrum of GO, and the peak for the C–O/C=O bond is almost absent. Compared with the spectrum of NGO, the peak of the C–O/C=O bond is also almost absent in the C 1s XPS spectrum of ZGO/N-rGO, which indicates that the hydrothermal synthesis significantly removed most oxygen-containing functional groups, thereby converting GO and NGO to rGO and N-rGO. In addition, the appearance of a peak at 286.20 eV in the respective C 1s XPS spectra of NGO and ZGO/N-rGO can be attributed to the C–N bond,[71] which indicates that nitrogen was successfully introduced into GO.

Fig. 7a shows that the XPS spectrum of the as-prepared NGO has a N peak (~400.0 eV),[55] whereas this peak does not appear in the XPS spectrum of GO (Fig. 7b), providing convincing evidence that nitrogen was successfully introduced into GO. The N 1s spectrum of NGO (Fig. 7c) comprises peaks corresponding to pyridine (398.45 eV) and pyrrole (400.68 eV).[55] Fig. 7d shows typical XPS survey spectra of $ZnGa_2O_4$, $ZnGa_2O_4$/N-rGO, and $ZnGa_2O_4$/rGO composites. The high-resolution spectra of the Zn 2p, Ga 3d, O 1s, and N 1s states of ZGO, ZGO/rGO, and ZGO/N-rGO are shown in Fig. 7e–h. The two peaks of pure $ZnGa_2O_4$ at 1024 and 1046.2 eV are attributed to Zn $2p_{3/2}$ and Zn $2p_{1/2}$, respectively, which are assigned to Zn^{2+} oxidation (Fig. 7e). The peaks with binding energies of 20.75 and 401.3 eV correspond to the Ga 3d state and the N 1s state of NO_3^-, respectively, in $ZnGa_2O_4$ (Fig. 7f and h).[72] The O 1s spectrum of pure $ZnGa_2O_4$ consists of two components: the peak with lower bind energy at 530.7 eV is ascribed to the lattice oxygen; the peak with higher bind energy at 532.6 eV is ascribed to the chemisorbed H_2O

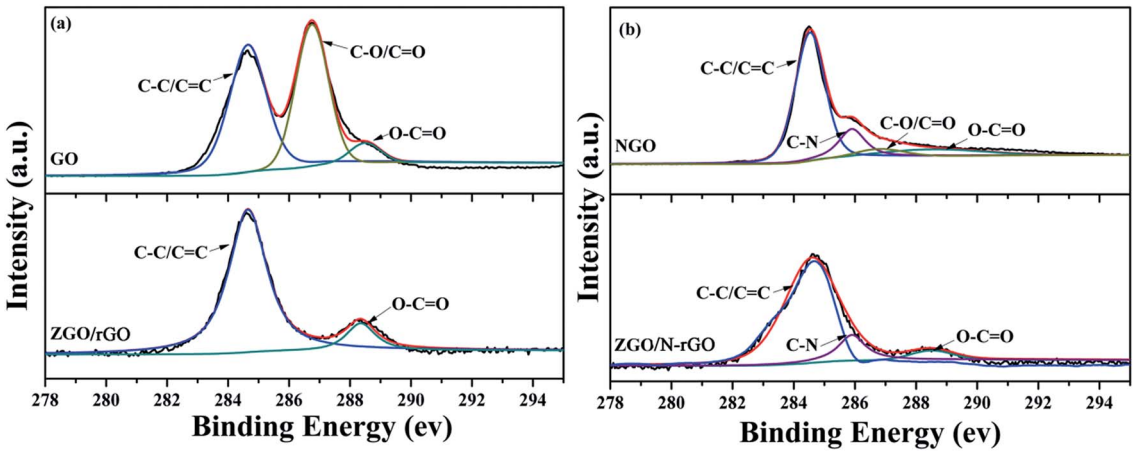

Fig. 6 C 1s XPS spectra of (a) GO, ZGO/rGO and (b) NGO, ZGO/N-rGO.

molecules or OH^- groups on the surface (Fig. 7g).[73] For the $ZnGa_2O_4$/rGO and $ZnGa_2O_4$/N-rGO composites, the peak corresponding to the Zn 2p state is blue shifted by 0.2 and 0.9 eV, respectively, while the Ga 3d peak is blue shifted by 0.05 and 0.2 eV, respectively, compared with the peak in the spectrum of pure $ZnGa_2O_4$. The O 1s peak of the $ZnGa_2O_4$/rGO and $ZnGa_2O_4$/N-rGO composites is shifted by 0.07 and 0.2 eV toward higher energy when compared with the peak in the spectrum of pure $ZnGa_2O_4$. The N 1s peak remains at the same binding energy for pure $ZnGa_2O_4$ and the $ZnGa_2O_4$/rGO and $ZnGa_2O_4$/N-rGO composites. Finally, a peak at 398.5 eV corresponding to pyridine from the C–N bond appears in the spectrum of the $ZnGa_2O_4$/N-rGO composite, which further confirms that nitrogen was successfully introduced into GO. These XPS spectra reveal the existence of chemical bonds between $ZnGa_2O_4$ and rGO or N-rGO in the composites, and the interfacial interaction between $ZnGa_2O_4$ and N-rGO was stronger than that in the $ZnGa_2O_4$/rGO composite.

The optical properties and band structures of the as-prepared samples were measured by UV-vis diffuse-reflectance spectroscopy and valence-band X-ray photoelectron spectroscopy (VB XPS). As shown in Fig. S4,† the absorption edge of the as-prepared $ZnGa_2O_4$ samples with $ZnGa_2O_4$ spheres of different sizes remained the same, indicating that the band gap (4.40 eV) estimated using Tauc plots of $(\alpha h\nu)^n$ *versus* photon energy ($h\nu$) following the Kubelka–Munk method[74] did not change. The absorption edge of the $ZnGa_2O_4$/rGO and $ZnGa_2O_4$/N-rGO composites also remained the same as that of bare $ZnGa_2O_4$ (Fig. 8a and b). However, when compared with the spectrum of pure $ZnGa_2O_4$, a wide absorption feature in the visible-light region appears in the spectra of the $ZnGa_2O_4$/rGO and $ZnGa_2O_4$/N-rGO composites. This can be attributed to the presence of carbon in the $ZnGa_2O_4$/rGO and $ZnGa_2O_4$/N-rGO composites, which reduced the reflection of light.[75] As shown in Fig. 8c, the position of the VB maxima of pure $ZnGa_2O_4$ and the $ZnGa_2O_4$/rGO and $ZnGa_2O_4$/N-rGO composites are same and located at about 3.36 eV, which means that the band gap and valance band did not change with the addition of rGO and N-rGO.

Photocatalytic activity of the $ZnGa_2O_4$, $ZnGa_2O_4$/rGO and $ZnGa_2O_4$/N-rGO composites

The photocatalytic activities of the samples for H_2 production were evaluated under irradiation by a 300 W xenon lamp and using sodium sulfite as a sacrificial agent. Fig. 9A shows a comparison of the photocatalytic activities of $ZnGa_2O_4$ with different sizes: $ZnGa_2O_4$-0, $ZnGa_2O_4$-0.25, $ZnGa_2O_4$-0.30, $ZnGa_2O_4$-0.35, and $ZnGa_2O_4$-0.40. The rate of H_2 production was poor when the $ZnGa_2O_4$-0 and $ZnGa_2O_4$-0.25 samples were made up of irregular particles. The photocatalytic activity for H_2 production was significantly enhanced when the $ZnGa_2O_4$ particles assembled to form nanospheres. As the diameter of the $ZnGa_2O_4$ spheres increased, the rate of H_2 production first increased, with a highest value of 38.94 μmol h^{-1} g^{-1} when the diameter of the $ZnGa_2O_4$ spheres reached 230 nm. Further increase in the diameter of the $ZnGa_2O_4$ spheres led to a decrease in the rate of H_2 evolution, which can be ascribed to the crystallinity, morphology, and BET surface area of the samples. The BET surface area of each sample is listed in the ESI Table S2.† It can be seen that $ZnGa_2O_4$-0 and $ZnGa_2O_4$-0.25 had large BET surface areas, but the two samples were made up of irregular particles and the crystallinity was low, resulting in low rates of H_2 evolution. When the amount of trisodium citrate used during synthesis was increased, the BET surface area of the samples decreased, but the morphology of $ZnGa_2O_4$-0.30, $ZnGa_2O_4$-0.35, and $ZnGa_2O_4$-0.40 was characterized by $ZnGa_2O_4$ particles assembling into nanospheres and the crystallinity was high, resulting in improved rates of H_2 evolution. Taking into account the above three factors, $ZnGa_2O_4$-0.35 showed the highest photocatalytic activity. Fig. 9B shows the photocatalytic activities for H_2 evolution of $ZnGa_2O_4$-0.25, $ZnGa_2O_4$-0.30, and $ZnGa_2O_4$-0.35 and their corresponding composites with rGO and N-rGO. The rates of H_2 evolution of the $ZnGa_2O_4$/rGO and $ZnGa_2O_4$/N-rGO composites dramatically improved when compared with that of $ZnGa_2O_4$, and $ZnGa_2O_4$/N-rGO had higher photocatalytic activity than $ZnGa_2O_4$/rGO. To investigate the effect of surface area on the photocatalytic activity for H_2 production, the rate of H_2 production as a function of the BET

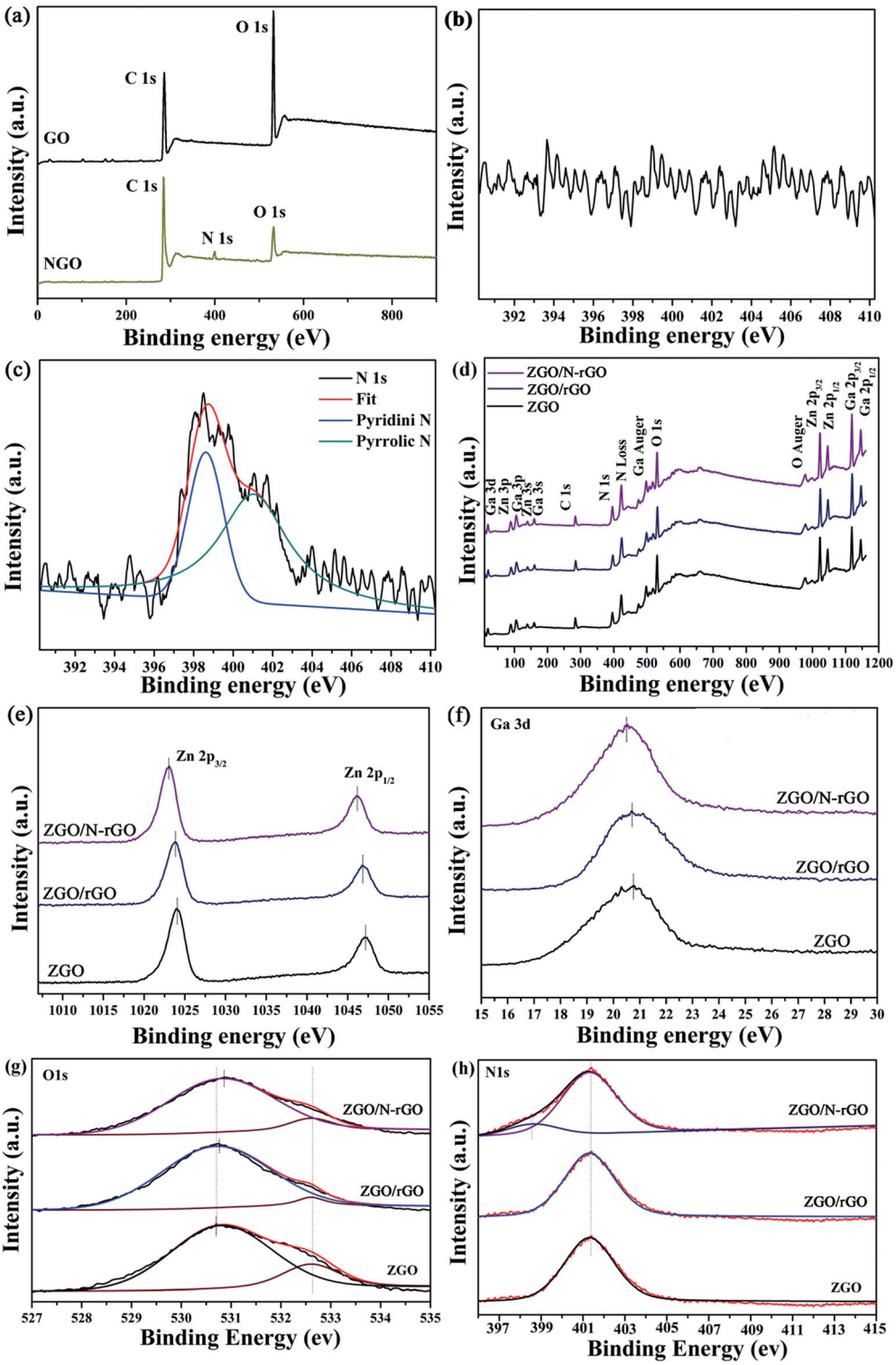

Fig. 7 XPS spectra for (a) survey of GO and NGO and the corresponding high-resolution spectra of N 1s of (b) GO and (c) NGO; (d) survey of ZGO, ZGO/rGO and ZGO/N-rGO; (e) Zn 2p of pure ZGO, ZGO/rGO and ZGO/N-rGO; (f) Ga 3d of ZGO, ZGO/rGO and ZGO/N-rGO; (g) O 1s of pure ZGO, ZGO/rGO and ZGO/N-rGO and (h) N 1s of ZGO, ZGO/rGO and ZGO/N-rGO.

surface area was examined (Fig. S5†). It can be seen that the BET surface area was not the cause of the dramatic improvement in the rate of H_2 evolution of the $ZnGa_2O_4$/rGO and $ZnGa_2O_4$/N-rGO composites when compared with that of $ZnGa_2O_4$. Thus, it can be concluded that because N-rGO possessed better electrical conductivity than rGO, it improved charge-carrier separation and transfer, resulting in the enhanced photocatalytic activities for H_2 production. Unlike pure $ZnGa_2O_4$, the $ZnGa_2O_4$/

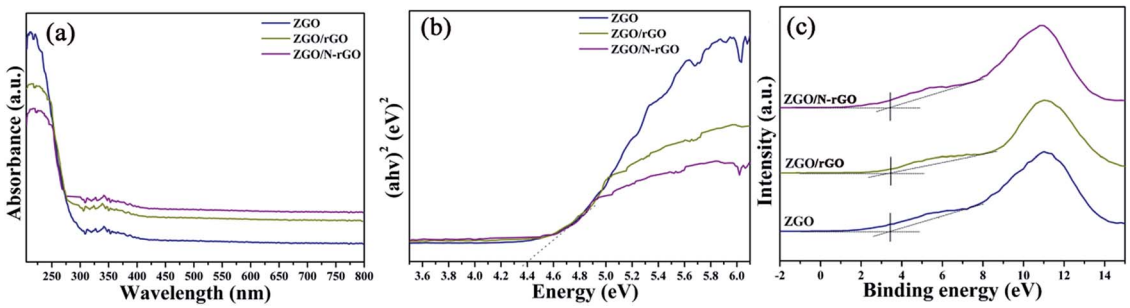

Fig. 8 (a) UV-vis diffuse reflectance spectra and (b) the plot of transformed Kubelka–Munk function *versus* the energy and (c) valence-band XPS spectra of ZGO, ZGO/rGO and ZGO/N-rGO.

rGO and $ZnGa_2O_4$/N-rGO composites showed the highest photocatalytic activity for H_2 production when the diameter of $ZnGa_2O_4$ spheres reached 80 nm, which was due to the intimate interfacial contact between the $ZnGa_2O_4$ spheres with suitable size and rGO or N-rGO. The results showed that using rGO or N-rGO as a catalyst support led to much higher ability for H_2 evolution. Moreover, a suitable size of $ZnGa_2O_4$ spheres was crucial to the optimization of interfacial contact and photocatalytic activity.

The stability of the composites is an important factor in their practical application as photocatalysts. To assess their suitability for practical use, we measured the photostability of the $ZnGa_2O_4$-0.30/N-rGO composites, and the result is shown in Fig. 10. The photocatalytic activity did not significantly diminish after six cycles of photocatalytic water splitting, which indicates that the composite exhibited excellent stability in photocatalytic H_2 generation from water splitting.

Mechanism accounting for the photocatalytic activity enhancement in $ZnGa_2O_4$, $ZnGa_2O_4$/rGO and $ZnGa_2O_4$/N-rGO composites

To investigate the charge-carrier separation and transfer in the samples, the photocurrent transient response (PCTR) and electrochemical impedance spectra (EIS) were measured. In the EIS, the semicircles in the Nyquist plots can be simulated well by an electrical equivalent circuits model. A smaller semicircle radius, corresponding to a lower charge-carrier transfer resistance value (R_{ct}), suggests a higher charge-carrier separation and transfer rate. Table S3† show R_{ct} value, which are calculated based on electrical equivalent circuits model. Fig. 11a and b show the PCTR and EIS of as-prepared $ZnGa_2O_4$ samples with different sizes. For $ZnGa_2O_4$-0 and $ZnGa_2O_4$-0.25, which consisted of irregular particles, the photocurrent densities were about 1.32 and 3.87 μA cm^{-2}, respectively. The photocurrent density of $ZnGa_2O_4$-0.30, $ZnGa_2O_4$-0.35, and $ZnGa_2O_4$-0.40 spheres were about 5.45, 6.4, and 6.27 μA cm^{-2}, respectively. The higher photocurrent in $ZnGa_2O_4$-0.35 and $ZnGa_2O_4$-0.40 suggests a higher charge-transfer rate, which promotes efficient separation of photogenerated electron–hole pairs and retards recombination of charge carriers. As shown in Fig. 11b, the Nyquist plots of $ZnGa_2O_4$-0.30, $ZnGa_2O_4$-0.35, and $ZnGa_2O_4$-0.40 show lower R_{ct} value when compared to those in the Nyquist plots of $ZnGa_2O_4$-0 and $ZnGa_2O_4$-0.25, indicating that the $ZnGa_2O_4$-0.30, $ZnGa_2O_4$-0.35 and $ZnGa_2O_4$-0.40 spheres had faster charge-transport rates. These results suggest that $ZnGa_2O_4$-0.35 and $ZnGa_2O_4$-0.4 had similar capability of charge-carrier separation and transfer because they had similar

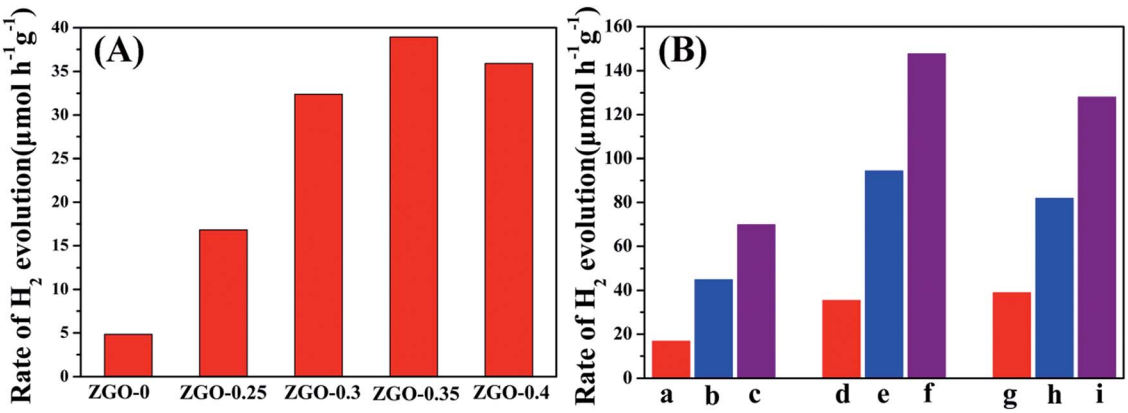

Fig. 9 Photocatalytic water splitting activity of (A) $ZnGa_2O_4$ with different size: $ZnGa_2O_4$-0, $ZnGa_2O_4$-0.25, $ZnGa_2O_4$-0.30, $ZnGa_2O_4$-0.35 and $ZnGa_2O_4$-0.40; (B) (a–c) $ZnGa_2O_4$-0.25, $ZnGa_2O_4$-0.25/rGO, $ZnGa_2O_4$-0.25/N-rGO; (d–f) $ZnGa_2O_4$-0.30, $ZnGa_2O_4$-0.30/rGO, $ZnGa_2O_4$-0.30/N-rGO; (g–i) $ZnGa_2O_4$-0.35, $ZnGa_2O_4$-0.35/rGO, $ZnGa_2O_4$-0.35/N-rGO. Reaction conditions: photocatalyst, 0.05 g; 100 mL 0.05 M Na_2SO_3 aqueous solution, a 300 W xenon lamp as the light source ($\lambda \geq 250$ nm) and reaction of 5 h.

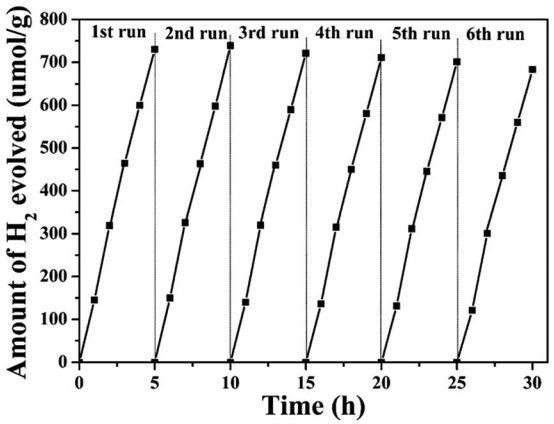

Fig. 10 Recycling test for the photocatalytic water splitting of the $ZnGa_2O_4$-0.30/N-rGO composites.

crystallinity. The PCTR and EIS results of $ZnGa_2O_4$ with different sizes are consistent with the results of photocatalytic water splitting activity. As shown in Fig. 11c, the $ZnGa_2O_4$/N-rGO composites showed increased current when compared to the $ZnGa_2O_4$/rGO composites, indicating that doping nitrogen into reduced graphene oxide increased the transfer rate of electrons from the conduction band of the semiconductor.[76] In addition, the photocurrent density of the $ZnGa_2O_4$-0.30/N-rGO composite was the highest, with a value of about 31.65 μA cm^{-2}, which can be attributed to the catalyst support N-rGO and the intimate interfacial contact between the $ZnGa_2O_4$ spheres with suitable size and N-rGO. Fig. 11d shows the EIS Nyquist plots of $ZnGa_2O_4$, $ZnGa_2O_4$/rGO, and $ZnGa_2O_4$/N-rGO. The R_{ct} value of the $ZnGa_2O_4$/N-rGO composites was lower, which further proved that nitrogen doping of reduced graphene oxide could enhance the charge-carrier separation and transfer for improved photocatalytic activity. The PCTR and EIS results of the $ZnGa_2O_4$/rGO and $ZnGa_2O_4$/N-rGO composites are consistent with the results of photocatalytic water splitting activity. This is because that rGO possessed high surface area and superior electrical conductivity, and N-rGO had better electrical conductivity than rGO. It is beneficial for the separation and transfer of photoinduced charge carriers.

In general, the PL spectrum is used to investigate the separation efficiency of photogenerated charge carriers in a photocatalyst. Fig. 12 shows PL spectra of as-prepared $ZnGa_2O_4$ samples with different size and $ZnGa_2O_4$/rGO and $ZnGa_2O_4$/N-rGO composites, obtained with an excitation wavelength of 310 nm. The spectra show a strong emission band in the 375–500 nm range, with the peak position at 421 nm, and it originated from the self-activation center of the octahedral Ga–O.[77] The weak band at 338 nm can be ascribed to absorption by $ZnGa_2O_4$.[57] As shown in Fig. 12a, both $ZnGa_2O_4$-0.35 and $ZnGa_2O_4$-0.40 exhibited a similar and weaker emission peak at

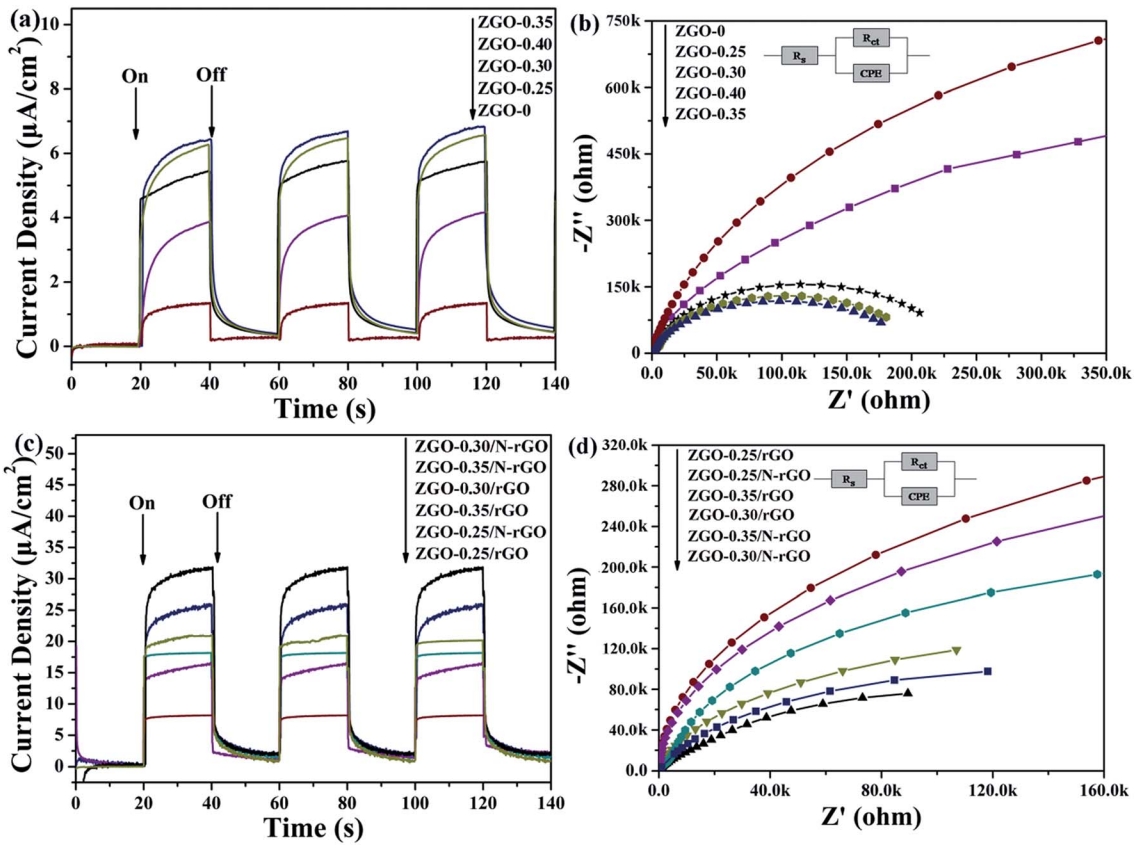

Fig. 11 Photocurrent responses and Nyquist plots of (a, b) $ZnGa_2O_4$ with different size: $ZnGa_2O_4$-0, $ZnGa_2O_4$-0.25, $ZnGa_2O_4$-0.30, $ZnGa_2O_4$-0.35 and $ZnGa_2O_4$-0.40 and (c, d) pure $ZnGa_2O_4$, $ZnGa_2O_4$/rGO and $ZnGa_2O_4$/N-rGO.

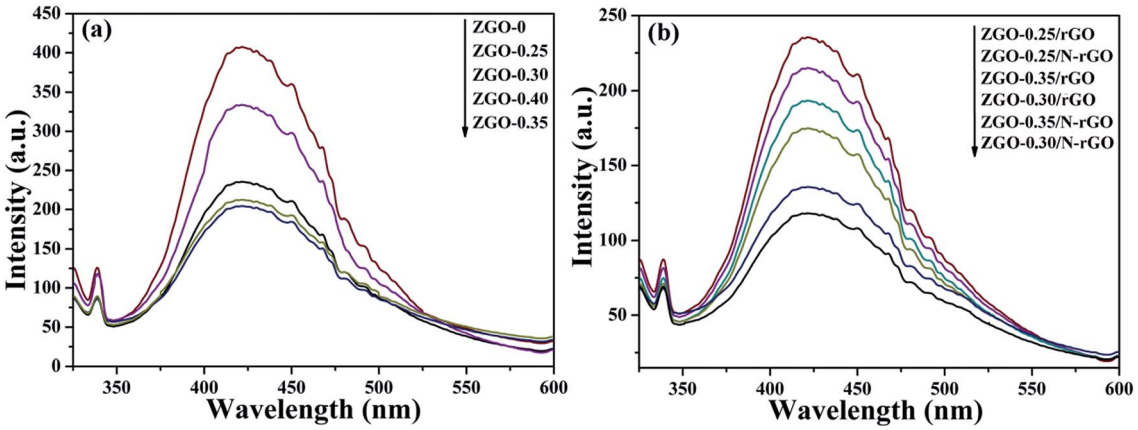

Fig. 12 PL spectra of (a) $ZnGa_2O_4$ with different size: $ZnGa_2O_4$-0, $ZnGa_2O_4$-0.25, $ZnGa_2O_4$-0.30, $ZnGa_2O_4$-0.35 and $ZnGa_2O_4$-0.40 and (b) pure $ZnGa_2O_4$, $ZnGa_2O_4$/rGO and $ZnGa_2O_4$/N-rGO. The spectra were obtained with an excitation wavelength of 310 nm.

the same position, indicating that high crystallinity was beneficial to suppressing the recombination of photogenerated electron–hole pairs. In the PL spectrum of $ZnGa_2O_4$/N-rGO, a weaker emission peak appears at the same position, indicating that the addition of N-rGO significantly suppressed the recombination of photogenerated electron–hole pairs. The PL results further confirmed that N-rGO possessed higher electrical conductivity than rGO and was beneficial for the separation and transfer of photoinduced charge carriers.

Based on the above results and discussion, we propose the mechanism for the photocatalytic reaction over $ZnGa_2O_4$/N-rGO composites as shown in Fig. 13. $ZnGa_2O_4$ can excite the electrons and produce photogenerated electron–hole pairs under ultraviolet light irradiation. Then the excited electrons on the conduction band (−1.04 V *vs.* NHE) of $ZnGa_2O_4$ could be easily transferred to the N-rGO sheets due to the lower Fermi level (−0.08 V *vs.* NHE)[54] of N-rGO compared to $ZnGa_2O_4$, which could inhibit electron–hole pairs recombination, leading to the enhanced photocatalytic activity. As a result, the photogenerated electrons gathered on the N-rGO sheets could effectively reduce H^+ to produce H_2 whereas the photogenerated holes could be sacrificed by oxidizing sulfite ions to sulfuric ions (Fig. 13). The N-rGO catalyst support possessed high electrical conductivity and the intimate interfacial contact between the $ZnGa_2O_4$ spheres with suitable size (80 nm) and N-rGO, which were beneficial for the separation of photoinduced charge carriers, resulting in enhanced photocatalytic H_2 generation from water splitting. For the $ZnGa_2O_4$ samples with different sizes, their crystallinity, morphology, and BET surface area were determining factors of their photocatalytic activities for H_2 production. Since a semiconductor with high crystallinity is beneficial for the transfer of photoinduced charge carriers.[56] As the crystallinity of $ZnGa_2O_4$ nanospheres increased with increasing diameter of the $ZnGa_2O_4$ spheres, the rate of H_2 production increased. When the crystallinity of $ZnGa_2O_4$-0.35 and $ZnGa_2O_4$-0.40 nanospheres were the similar, the BET surface area was the factor that resulted in a decrease of the rate of H_2 evolution for the $ZnGa_2O_4$-0.40 nanospheres. Thus, based on the combined effect of the crystallinity, morphology and BET surface area $ZnGa_2O_4$-0.35 showed the highest photocatalytic activity for H_2 production when the diameter of $ZnGa_2O_4$ spheres reached 230 nm.

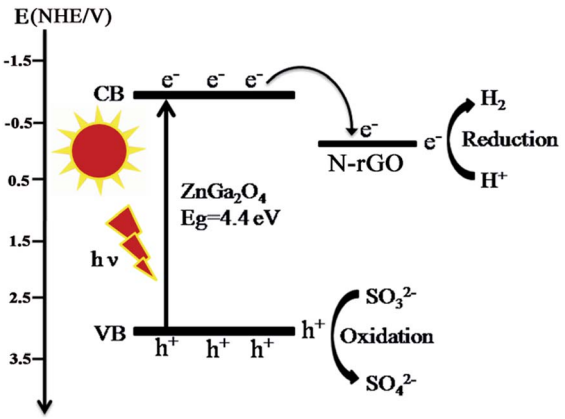

Fig. 13 Schematic diagram of photogenerated electrons transfer between $ZnGa_2O_4$ and N-rGO.

Conclusion

In summary, we successfully synthesized size-controlled $ZnGa_2O_4$ nanospheres by adjusting the amount of surfactant trisodium citrate, and assembled $ZnGa_2O_4$ on the 2D platform of N-doped reduced graphene oxide (N-rGO) sheet through conventional and efficient hydrothermal method, during which the intimate interfacial contact between $ZnGa_2O_4$ and the N-rGO sheet are achieved. The $ZnGa_2O_4$/N-rGO composites showed remarkably improved photocatalytic performance under ultraviolet light irradiation. The highest H_2 evolution rate reached 147.61 μmol h^{-1} g^{-1} with an apparent quantum efficiency of 3.2% at 365 nm. The H_2-production rate is almost 4.2 times of that of pure $ZnGa_2O_4$ measured at the same conditions. The excellent photocatalytic H_2-evolution activity of the $ZnGa_2O_4$/N-rGO composites can be attributed to the presence of N-rGO and the intimate interfacial contact between $ZnGa_2O_4$

nanospheres with suitable size (80 nm) and N-rGO. N-rGO acted as a catalyst support and electron sink for promoting charge separation and transfer. The size of $ZnGa_2O_4$ nanospheres was related to the strong interfacial contact between $ZnGa_2O_4$ and N-rGO. This work provides a new strategy to improve the photocatalytic activity of $ZnGa_2O_4$ and offers new insight into the design and development of graphene-based composites for various applications.

Conflicts of interest

There are no conflicts to declare.

Acknowledgements

This work was supported by the National Natural Science Foundation of China (Grant No. 21173131 and 21771119) and the Taishan Scholar Project of Shandong Province.

Notes and references

1 J. O. M. Bockris, *Int. J. Hydrogen Energy*, 2002, **27**, 731–740.
2 D. Ravelli, D. Dondi, M. Fagnoni and A. Albini, *Chem. Soc. Rev.*, 2009, **38**, 1999–2011.
3 J. A. Turner, *Science*, 1999, **285**, 687–689.
4 W. Li, X. Wang, D. Xiong and L. Liu, *Int. J. Hydrogen Energy*, 2016, **41**, 9344–9354.
5 X. Wang, W. Li, D. Xiong, D. Y. Petrovykh and L. Liu, *Adv. Funct. Mater.*, 2016, **26**, 4067–4077.
6 D. Xiong, W. Li, X. Wang and L. Liu, *Nanotechnology*, 2016, **27**, 375401.
7 W. Li, X. Gao, X. Wang, D. Xiong, P.-P. Huang, W.-G. Song, X. Bao and L. Liu, *J. Power Sources*, 2016, **330**, 156–166.
8 W. Li, X. Gao, D. Xiong, F. Xia, J. Liu, W.-G. Song, J. Xu, S. M. Thalluri, M. F. Cerqueira, X. Fu and L. Liu, *Chem. Sci.*, 2017, **8**, 2952–2958.
9 W. Li, X. Gao, D. Xiong, F. Wei, W.-G. Song, J. Xu and L. Liu, *Adv. Energy Mater.*, 2017, **7**, 1602579.
10 W. Li, D. Xiong, X. Gao, W.-G. Song, F. Xia and L. Liu, *Catal. Today*, 2017, **287**, 122–129.
11 F. E. Osterloh, *Chem. Soc. Rev.*, 2013, **42**, 2294–2320.
12 A. Kudo and Y. Miseki, *Chem. Soc. Rev.*, 2009, **38**, 253–278.
13 R. M. Navarro, M. C. Alvarez-Galván, J. A. Villoria de la Mano, S. M. Al-Zahrani and J. L. G. Fierro, *Energy Environ. Sci.*, 2010, **3**, 1865–1882.
14 L. Qi, J. Yu and M. Jaroniec, *Phys. Chem. Chem. Phys.*, 2011, **13**, 8915–8923.
15 J. Zhang, J. Yu, M. Jaroniec and J. R. Gong, *Nano Lett.*, 2012, **12**, 4584–4589.
16 L. Cao, D. Chen, W. Li and R. A. Caruso, *ACS Appl. Mater. Interfaces*, 2014, **6**, 13129–13137.
17 Y. Yu, C. Cao, W. Li, P. Li, J. Qu and W. Song, *Nano Res.*, 2012, **5**, 434–442.
18 T. Hisatomi, J. Kubota and K. Domen, *Chem. Soc. Rev.*, 2014, **43**, 7520–7535.
19 Y. Inoue, *Energy Environ. Sci.*, 2009, **2**, 364–386.
20 S. C. Yan, S. X. Ouyang, J. Gao, M. Yang, J. Y. Feng, X. X. Fan, L. J. Wan, Z. S. Li, J. H. Ye, Y. Zhou and Z. G. Zou, *Angew. Chem., Int. Ed.*, 2010, **49**, 6400–6404.
21 L. Liu, J. Huang, L. Cao, J. Wu, J. Fei, H. Ouyang, F. Ma and C. Zhou, *Mater. Lett.*, 2013, **95**, 160–163.
22 N. Kumagai, L. Ni and H. Irie, *Chem. Commun.*, 2011, **47**, 1884–1886.
23 X. Xu, A. K. Azad and J. T. S. Irvine, *Catal. Today*, 2013, **199**, 22–26.
24 C. Zeng, T. Hu, N. Hou, S. Liu, W. Gao, R. Cong and T. Yang, *Mater. Res. Bull.*, 2015, **61**, 481–485.
25 R. Marschall, *Adv. Funct. Mater.*, 2014, **24**, 2421–2440.
26 L. J. Zhang, R. Zheng, S. Li, B. K. Liu, D. J. Wang, L. L. Wang and T. F. Xie, *ACS Appl. Mater. Interfaces*, 2014, **6**, 13406–13412.
27 X. Li, Y. Feng, M. Li, W. Li, H. Wei and D. Song, *Adv. Funct. Mater.*, 2015, **25**, 6858–6866.
28 K. Trzciński, M. Szkoda, M. Sawczak, J. Karczewski and A. Lisowska-Oleksiak, *Appl. Surf. Sci.*, 2016, **385**, 199–208.
29 D. Lang, F. Cheng and Q. Xiang, *Catal. Sci. Technol.*, 2016, **6**, 6207–6216.
30 H. Yu, P. Xiao, P. Wang and J. Yu, *Appl. Catal., B*, 2016, **193**, 217–225.
31 X. Wang, T. Li, R. Yu, H. Yu and J. Yu, *J. Mater. Chem. A*, 2016, **4**, 8682–8689.
32 F. Cheng, H. Yin and Q. Xiang, *Appl. Surf. Sci.*, 2017, **391**, 432–439.
33 J. Wen, J. Xie, X. Chen and X. Li, *Appl. Surf. Sci.*, 2017, **391**, 72–123.
34 A. K. Geim and K. S. Novoselov, *Nat. Mater.*, 2007, **6**, 183–191.
35 M.-Q. Yang, N. Zhang, M. Pagliaro and Y.-J. Xu, *Chem. Soc. Rev.*, 2014, **43**, 8240–8254.
36 N. Zhang, M.-Q. Yang, S. Liu, Y. Sun and Y.-J. Xu, *Chem. Rev.*, 2015, **115**, 10307–10377.
37 F. Perreault, A. Fonseca de Faria and M. Elimelech, *Chem. Soc. Rev.*, 2015, **44**, 5861–5896.
38 X. Li, J. Yu, S. Wageh, A. A. Al-Ghamdi and J. Xie, *Small*, 2016, **12**, 6640–6696.
39 Y. Xu, Y. Mo, J. Tian, P. Wang, H. Yu and J. Yu, *Appl. Catal., B*, 2016, **181**, 810–817.
40 Q. Xiang, F. Cheng and D. Lang, *ChemSusChem*, 2016, **9**, 996–1002.
41 M. Liu, F. Li, Z. Sun, L. Xu, Y. Song and A. Munventwali, *RSC Adv.*, 2015, **5**, 47314–47318.
42 G. P. Singh, K. M. Shrestha, A. Nepal, K. J. Klabunde and C. M. Sorensen, *Nanotechnology*, 2014, **25**, 265701.
43 Q. Xiang, J. Yu and M. Jaroniec, *Nanoscale*, 2011, **3**, 3670–3678.
44 X. Tang, W. Chen, Z. Zu, Z. Zang, M. Deng, T. Zhu, K. Sun, L. Sun and J. Xue, *Nanoscale*, 2015, **7**, 18498–18503.
45 Y. Zhu, S. Murali, W. Cai, X. Li, J. W. Suk, J. R. Potts and R. S. Ruoff, *Adv. Mater.*, 2010, **22**, 3906–3924.
46 L. Ci, L. Song, C. Jin, D. Jariwala, D. Wu, Y. Li, A. Srivastava, Z. F. Wang, K. Storr, L. Balicas, F. Liu and P. M. Ajayan, *Nat. Mater.*, 2010, **9**, 430–435.
47 X. Wang, X. Li, L. Zhang, Y. Yoon, P. K. Weber, H. Wang, J. Guo and H. Dai, *Science*, 2009, **324**, 768–771.

48 M. Deifallah, P. F. McMillan and F. Corà, *J. Phys. Chem. C*, 2008, **112**, 5447–5453.
49 Y. Li, Z. Zhou, P. Shen and Z. Chen, *ACS Nano*, 2009, **3**, 1952–1958.
50 D. Deng, X. Pan, L. Yu, Y. Cui, Y. Jiang, J. Qi, W.-X. Li, Q. Fu, X. Ma, Q. Xue, G. Sun and X. Bao, *Chem. Mater.*, 2011, **23**, 1188–1193.
51 A. L. M. Reddy, A. Srivastava, S. R. Gowda, H. Gullapalli, M. Dubey and P. M. Ajayan, *ACS Nano*, 2010, **4**, 6337–6342.
52 H. Xu, J. Xiao, B. Liu, S. Griveau and F. Bedioui, *Biosens. Bioelectron.*, 2015, **66**, 438–444.
53 Q. Wu, L. Liao, Q. Zhang, Y. Nie, J. Xiao, S. Wang, S. Dai, Q. Gao, Y. Zhang, X. Sun, B. Liu and Y. Tang, *Electrochim. Acta*, 2015, **158**, 42–48.
54 C. Liu, L. Zhang, R. Liu, Z. Gao, X. Yang, Z. Tu, F. Yang, Z. Ye, L. Cui, C. Xu and Y. Li, *Journal*, 2016, **656**, 24–32.
55 Z.-L. Wang, J.-M. Yan, Y.-F. Zhang, Y. Ping, H.-L. Wang and Q. Jiang, *Nanoscale*, 2014, **6**, 3073–3077.
56 K. Lin, B. Ma, W. Su and W. Liu, *Appl. Surf. Sci.*, 2013, **286**, 61–65.
57 Y. Zhang, Z. Wu, D. Geng, X. Kang, M. Shang, X. Li, H. Lian, Z. Cheng and J. Lin, *Adv. Funct. Mater.*, 2014, **24**, 6581–6593.
58 L. Liu, C. Dong, K.-L. Wu, Y. Ye and X.-W. Wei, *Mater. Lett.*, 2014, **129**, 170–173.
59 Z. Mou, Y. Wu, J. Sun, P. Yang, Y. Du and C. Lu, *ACS Appl. Mater. Interfaces*, 2014, **6**, 13798–13806.
60 Q. Mi, D. Chen, J. Hu, Z. Huang and J. Li, *Chin. J. Catal.*, 2013, **34**, 2138–2145.
61 R. Rao, R. Podila, R. Tsuchikawa, J. Katoch, D. Tishler, A. M. Rao and M. Ishigami, *ACS Nano*, 2011, **5**, 1594–1599.
62 Z. Le-Sheng, L. Wei, C. Zhi-Min and S. Wei-Guo, *J. Phys. Chem. C*, 2009, **113**, 20594–20598.
63 W. Li, L.-S. Zhang, Q. Wang, Y. Yu, Z. Chen, C.-Y. Cao and W.-G. Song, *J. Mater. Chem.*, 2012, **22**, 15342.
64 T. N. Lambert, C. A. Chavez, B. Hernandez-Sanchez, P. Lu, N. S. Bell, A. Ambrosini, T. Friedman, T. J. Boyle, D. R. Wheeler and D. L. Huber, *J. Phys. Chem. C*, 2009, **113**, 19812–19823.
65 S. Stankovich, D. A. Dikin, R. D. Piner, K. A. Kohlhaas, A. Kleinhammes, Y. Jia, Y. Wu, S. T. Nguyen and R. S. Ruoff, *Carbon*, 2007, **45**, 1558–1565.
66 Y. Wang, J. Yu, W. Xiao and Q. Li, *J. Mater. Chem. A*, 2014, **2**, 3847–3855.
67 P.-G. Ren, D.-X. Yan, X. Ji, T. Chen and Z.-M. Li, *Nanotechnology*, 2011, **22**, 055705.
68 Y. Zheng, Y. Jiao, L. Ge, M. Jaroniec and S. Z. Qiao, *Angew. Chem., Int. Ed.*, 2013, **52**, 3110–3116.
69 R. S. Dey, S. Hajra, R. K. Sahu, C. R. Raj and M. K. Panigrahi, *Chem. Commun.*, 2012, **48**, 1787–1789.
70 W. Tu, Y. Zhou, Q. Liu, S. Yan, S. Bao, X. Wang, M. Xiao and Z. Zou, *Adv. Funct. Mater.*, 2013, **23**, 1743–1749.
71 J. Che, L. Shen and Y. Xiao, *J. Mater. Chem.*, 2010, **20**, 1722–1727.
72 T. Zheng, Y. Xia, X. Jiao, T. Wang and D. Chen, *Nanoscale*, 2017, **9**, 3206–3211.
73 L. Armelao, G. Bottaro, C. Maccato and E. Tondello, *Dalton Trans.*, 2012, **41**, 5480–5485.
74 N. M. Nursam, J. Z. Y. Tan, X. Wang, W. Li, F. Xia and R. A. Caruso, *ChemistrySelect*, 2016, **1**, 4868–4878.
75 X.-Y. Zhang, H.-P. Li, X.-L. Cui and Y. Lin, *J. Mater. Chem.*, 2010, **20**, 2801–2806.
76 B. Appavu, K. Kannan and S. Thiripuranthagan, *J. Ind. Eng. Chem.*, 2016, **36**, 184–193.
77 S. Y. Bae, J. Lee, H. Jung, J. Park and J.-P. Ahn, *J. Am. Chem. Soc.*, 2005, **127**, 10802–10803.

